nature communications

Article

https://doi.org/10.1038/s41467-025-63166-y

De novo design of hypercompact transcript degraders by engineering substrate-specific toxins and Cas6-CBS system

Received: 16 November 2024

Accepted: 11 August 2025

Published online: 26 September 2025

Check for updates

Pin-Ru Chen[1], Pei-Pei Qin[1], Ya-Nan Wang[1], Peng-Fu Liu[1], Xin-Yue Zhang[2], Tao Qian[1], Bang-Ce Ye[2] & Bin-Cheng Yin[2,3]

Artificial assembly of small functional proteins provides effective strategies for development of compact RNA degradation systems, which overcome the challenges associated with delivery. Here, we excavate and evolve three small toxin endoribonucleases with simple RNA cleavage motifs (barnase, MqsR, and MaZF), and integrate catalytically dead Cas6 (dCas6) along with its cognate stem-loop RNA (Cas6 binding site, termed CBS) from *Escherichia coli* (*E. coli*) to create hypercompact transcript degraders (317 ~ 430 amino acids), named STAR (small toxin- and d*Ec*Cas6-CBS-based RNA degraders). We experimentally find that CBS can be fine-tuned for *Ec*Cas6 processing but exhibits high conservatism in *Ec*Cas6 and d*Ec*Cas6 binding, laying a foundation for the design of CBS guides to effectively recruit d*Ec*Cas6-toxins. STAR exhibits high-efficiency knockdown of both cytoplasmic and nuclear transcripts in the tested mammalian cells, with significantly reduced off-target activities compared to established CRISPR and RNA interference (RNAi) technologies. Moreover, the small size of STAR enables delivery via a single adeno-associated virus (AAV) for ease of multiplex RNA knockdown, including effective silencing of the oncogenic RNA *MYC* in human cancer cells. Together, STAR unlocks new territory for employing toxin to design miniature, efficacious and safer RNA degraders.

Gene expression regulation at the RNA-level interventions is tempting due to its reversibility, lower risk of permanent genomic alterations, and broader targeting accessibility[1,2]. RNA knockdown technology, particularly small interfering RNAs (siRNAs) that harness the natural cellular process of RNAi, is a widely used method in molecular biology and therapeutics[3]. However, RNAi has notable limitations, including its inapplicability in prokaryotes, eukaryotic nuclei, or cytoplasmic compartments lacking RNAi machinery[4,5]. Additionally, RNAi suffers from poor controllability and off-target effects[6,7], prompting the search for alternative approaches. Recent advancements in biotechnology have spurred the development of new RNA knockdown tools with enhanced flexibility and potency[8,9]. Among these, certain CRISPR-Cas systems possessing natural RNA-targeting and ribonuclease activities, such as the class 1 type III CRISPR-Csm complex[10], the single-protein type III Cas7-11[11], and the class 2 type VI Cas13 families[12–14], have been leveraged as programmable RNA degraders with improved specificity and expanded targeting capabilities in eukaryotic cells. However, these CRISPR-Cas systems, along with their essential expression modules, often approach or exceed the packaging limits of common delivery vectors, such as AAV (~4.7 kilobases)[15–17], posing a major obstacle for

[1]Institute of Engineering Biology and Health, Collaborative Innovation Center of Yangtze River Delta Region Green Pharmaceuticals, College of Pharmaceutical Sciences, Zhejiang University of Technology, Hangzhou, Zhejiang, China. [2]Lab of Biosystem and Microanalysis, State Key Laboratory of Bioreactor Engineering, Shanghai Collaborative Innovation Center for Biomanufacturing Technology, East China University of Science and Technology, Shanghai, China. [3]School of Chemistry and Chemical Engineering, Shihezi University, Shihezi, Xinjiang, China. e-mail: bcye@ecust.edu.cn; binchengyin@ecust.edu.cn

effective therapeutic delivery. To address these size constraints, considerable efforts have focused on downsizing CRISPR toolkits. For instance, researchers have identified naturally occurring small Cas enzymes like Cas13X.1 (775 amino acids)[18] and Cas13bt1 (790 amino acids)[19], which are smaller than *Rfx*Cas13d (Cas13d from *Ruminococcus flavefaciens XPD3002*, 967 amino acids) but generally exhibit lower efficiency. Structural engineering guided by AlphaFold predictions has also enabled the creation of a mini version of *Rfx*Cas13d (690 amino acids) by excising non-functional regions[20]. However, this downsizing process is intricate, labor-intensive, and often limited in achieving substantial size reductions while preserving functionality.

The fusion of smaller RNA-binding proteins with ribonucleases to artificially fabricate hypercompact RNA degradation systems presents a promising avenue in the evolution of RNA knockdown technologies, not only elegantly tackling the delivery issue, but also enhancing design flexibility and expanding the repertoire of tools for RNA manipulation[21,22]. For instance, Dickinson et al. developed a modular CRISPR Cas-inspired RNA-targeting system (CIRTS, 432 amino acids) for direct transcript degradation by fusing a smaller version of hairpin-binding U1A protein (TBP6.7) with a non-specific ribonuclease Pin domain of SMG6, along with a guide RNA (gRNA) that interacts with both the hairpin binding protein and the target RNA[23]. However, despite the proof-of-concept success, the efficiency of RNA knockdown achieved with CIRTS is relatively modest, averaging around 40–50% for most tested targets. Additionally, the reliance on manganese ions (Mn^{2+}) for the catalytic hydrolysis activity of the Pin nuclease poses practical challenges, as Mn^{2+} levels vary significantly across different cells and tissues. The requirement of an extra nonspecific single-stranded RNA (ssRNA)-binding protein, open reading frame 5 (ORF5), to stabilize the guide RNA (gRNA) in CIRTS further increases complexity and the overall size of the degrader. These limitations highlight the ongoing efforts to enhance efficiency, reduce dependence on auxiliary components, and streamline the design of artificial RNA degradation systems for broader practical applications.

Prokaryotic toxins, a class of tiny ribonucleases, are widespread in bacteria and categorized into eight subgroups based on the nature of their cognate antitoxins[24,25]. Type II ribosome-independent toxins, in particular, enable highly efficient RNA digestion in a sequence-specific manner without requiring auxiliary components[26], making them particularly appealing for developing advanced RNA degradation systems that surpass the limitations of the conventional Pin nuclease. Notably, the toxins with cleavage motifs shorter than four nucleotides, a feature often found in cellular RNAs, show potential as general ribonucleases. However, this characteristic also raises concerns regarding off-target effects and cytotoxicity[27]. Therefore, it is imperative to develop engineering strategies to improve their specificity and safety.

Additionally, utilizing a small RNA-binding protein with a higher affinity for its target motif than that of TBP6.7 and its hairpin RNA, which shows nanomolar-level affinity in CIRTS, could further boost RNA knockdown efficiency. This enhancement likely results from the extended residence time of the fused ribonuclease on the RNA substrate, allowing for prolonged interaction and cleavage. A notable example of such a protein is Cas6, a core component of type I-E CRISPR complex, consisting of approximately 200 amino acids. Cas6 binds to its cognate stem-loop RNA (CBS, 20–30 nucleotides (nt)) with an exceptionally high affinity in the picomolar range[28,29], and possesses endoribonuclease activity, enabling cleavage at a defined site within the 3′ region of the CBS[30,31]. This unique nuclease property of Cas6 has been harnessed for RNA degradation by inserting the CBS into target gene loci[32,33]. However, this approach adds procedural complexity and may risk interfering with normal RNA functions or even causing unintended degradation[34].

In this study, we engineer toxins into more specific and safer ribonucleases and integrate them with the nuclease-inactive Cas6-CBS system derived from *E. coli* to develop a hypercompact RNA degradation system, named STAR (small toxin- and d*Ec*Cas6-CBS-based RNA degrader). Through the engineering of barnase, MqsR, and MaZF toxins, we generate a series of d*Ec*Cas6-toxin variants. Eight variants, exhibiting optimal ribonuclease activities and minimal cytotoxicity, are selected using a rapid dual-fluorescence reporter system and cytotoxicity assays in mammalian cells. We refine CBS sequence features critical for *Ec*Cas6 cleavage and stable *Ec*Cas6/d*Ec*Cas6 binding, designing CBS guides to direct d*Ec*Cas6-toxin targeting. Our results reveal that three toxin variants show distinct dependencies on the ORF5 element. Notably, ORF5-d*Ec*Cas6-barnase 11 (430 amino acids), d*Ec*Cas6-MqSR 20 (317 amino acids), and d*Ec*Cas6-MaZF 28 (330 amino acids) demonstrate knockdown efficiencies of cytoplasmic mRNAs comparable to those achieved by *Rfx*Cas13d[13]- and short hairpin RNA (shRNA)[5]-mediated methods. These three d*Ec*Cas6-toxin fusions also effectively degrade nuclear noncoding RNAs (ncRNAs). RNA sequencing reveals that d*Ec*Cas6-MaZF 28 exhibits minimal off-target effects, outperforming *Rfx*Cas13d and shRNA methods. Finally, AAV-packaged STAR achieves multiplexed knockdown of endogenous transcripts and effective degradation of the oncogenic RNA *MYC* in hepatocellular carcinoma line G2 (HepG2) cells, underscoring its potential for therapeutic applications.

Results

Diminishing the RNA cleavage activity of d*Ec*Cas6-toxins through protein engineering

To fabricate safer d*Ec*Cas6-toxins, we first sought to refine the RNA cleavage activity of the toxin nucleases via mutagenesis. Our aim was to identify variants that exhibit minimal off-target effects in the unbound state, thus reducing nonspecific degradation from random collisions, while maintaining high on-target cleavage efficiency when guided by CBS recruitment. To achieve this, we designed a dual-fluorescence reporter plasmid, featuring a blue fluorescent protein (BFP) gene to monitor off-target activity and a green fluorescent protein (GFP) gene fused to a wild-type CBS (wtCBS) at the 5′ untranslated region (UTR) to evaluate on-target degradation activity (Fig. 1a). In this system, pronounced BFP fluorescence signifies low off-target cleavage activity, while reduced GFP fluorescence indicates effective on-target cleavage by d*Ec*Cas6-toxin targeting and degrading wtCBS-GFP mRNA.

We selected the wild-type barnase (wtbarnase) from *Bacillus amyloliquefaciens* (*B. amyloliquefaciens*) for engineering due to its simple cleavage motif (G^N, where the ^ symbol denotes the cleavage site and N indicates a preference for A > G > C > U)[26]. Previous structural and biochemical studies have identified two critical amino acid residues (E73 and H102, denoted in cyan, Fig. 1b) essential for RNA cleavage, and eight residues (K27, F56, N58, R59, E60, R83, R87, and Y103, denoted in blue, Fig. 1b) important for substrate RNA binding[35,36]. We first mutated the catalytic residues to alanine and fused them to d*Ec*Cas6 with a nuclear export sequence (NES) and a flexible $(GGS)_3$ linker for proper protein localization and functionality. During the construction of barnase variant plasmids, we encountered cloning challenges with wtbarnase and barnase variant (E73A), likely due to the leaky expression of this highly active ribonuclease, which caused lethal toxicity in *E. coli* DH5α host cells. Subsequently, we individually co-transfected the two d*Ec*Cas6-barnase variants (H102A and E73A/H102A, referred to as #1 and #2) into human embryonic kidney (HEK293T) cells, along with the dual-fluorescence reporter plasmids. Fluorescence intensities were measured using flow cytometry 48 hours post-transfection. Despite mutations in the active site, the barnase variants (#1 and #2) still exhibited substantial off-target activity (Fig. 1c, gray zone), as indicated by moderate BFP signal. To further improve specificity, we explored combinations of mutations in the substrate-binding residues based on barnase 2, generating 14 variants (referred to as #3 to #16, Fig. 1c, gray zone). Our hypothesis was that reducing substrate binding would decrease the residence time of the barnase variants on the substrate, thereby minimizing off-target activity. As

https://doi.org/10.1038/s41467-025-63166-y

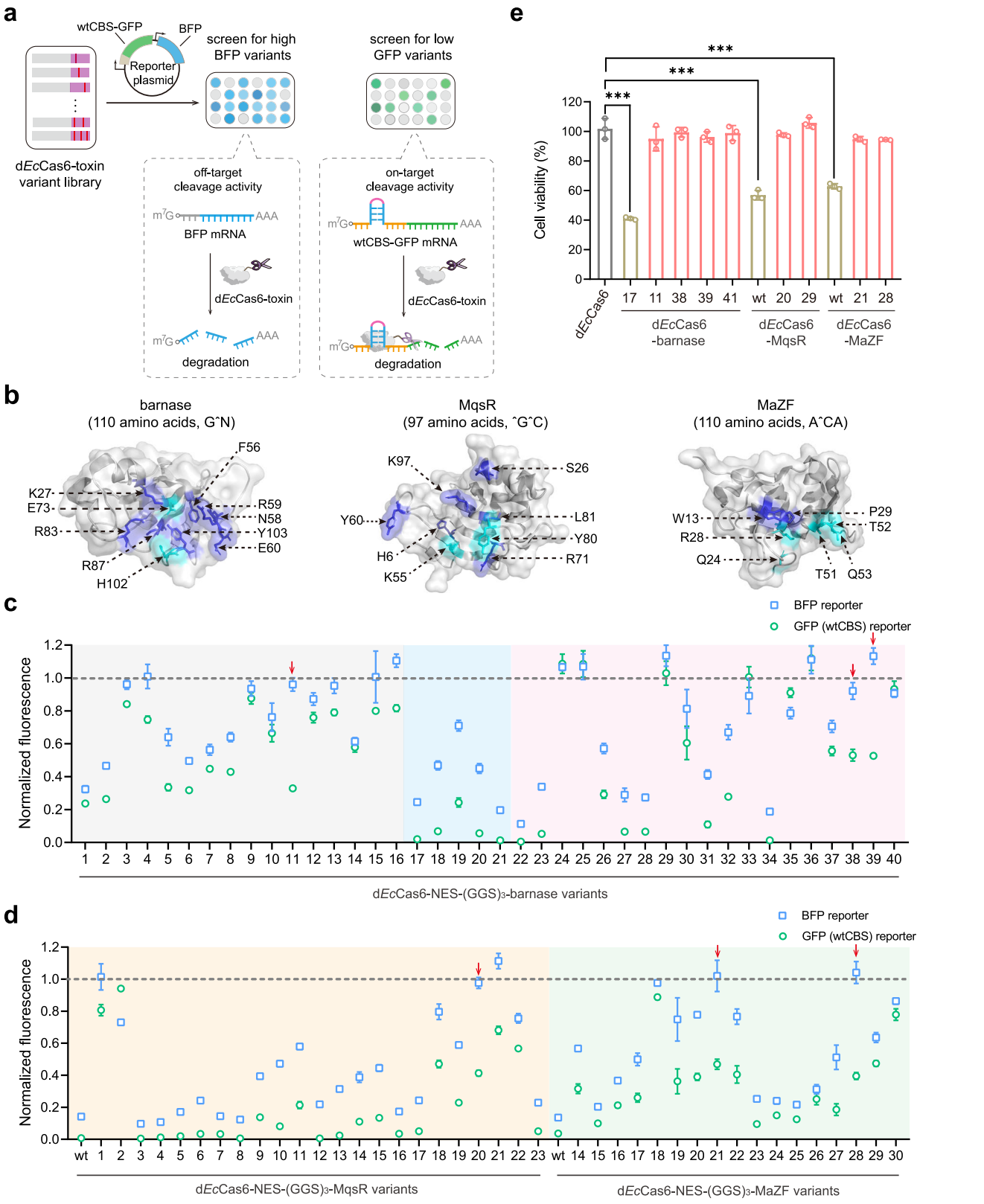

expected, mutations in the substrate-binding residues led to a reduction in off-target effects. Notably, barnase 11 (N58D/R59A/E73A/H102A) exhibited high BFP and low GFP fluorescence signals, indicative of minimal off-target effects on BFP mRNA and effective on-target degradation of GFP mRNA.

We also investigated a barnase variant (K27A/N58D/R59A/E73A, referred to as #17) reported in a previous study[37]. Unexpectedly, during the clone construction, barnase 17 generated three additional variants with mutations or deletions at the C terminus (#18 to #20, Supplementary Fig. 1). As shown in the blue zone in Fig. 1c, barnase 17 showed the highest off-target and on-target activities, as indicated by lowest BFP and GFP signals. In contrast, barnases 18 to 20 exhibited reduced nonspecific activities (higher BFP signals) compared to barnase 17, highlighting the role of C-terminal amino acids in activity

Fig. 1 | Rational engineering of toxin endoribonucleases with minimal off-target and high on-target cleavage activities. a Schematic of the working principle of the dual-fluorescence reporter system for screening d*Ec*Cas6-toxin variants. **b** Active sites of barnase (PDB ID: 1BGS), MqsR (PDB ID: 3HI2), and MaZF (PDB ID: 5CO7). Residues essential for substrate binding and cleavage are highlighted in blue and cyan, respectively. **c** Flow cytometry analysis of BFP and GFP transcript degradation in HEK293T cells treated with d*Ec*Cas6-NES-$(GGS)_3$-barnase variants. Results are normalized against a control group treated with d*Ec*Cas6. **d** Flow cytometry analysis of BFP and GFP transcript degradation in HEK293T cells treated with d*Ec*Cas6-NES-$(GGS)_3$-MqsR and d*Ec*Cas6-NES-$(GGS)_3$-MaZF variants, respectively. Results are normalized against a control group treated with d*Ec*Cas6. wt refers to wide-type MqsR or MaZF. **e** Assessment of HEK293T cell viability 48 h post-transfection with d*Ec*Cas6-toxins using a CCK-8 assay. Significance determined by two-tailed Student's *t* test ($P_{left} = 0.0001$; $P_{middle} = 0.0006$; $P_{right} = 0.0007$). $^{****}P < 0.0001$, $^{***}P < 0.001$, $^{**}P < 0.01$, $^{*}P < 0.05$. Data are mean ± s.e.m. of $n = 3$ biological replicates. Source data are provided as a Source data file.

modulation. These results suggested that DH5α cell-induced mutagenesis during the clone process enriched the mutant library, pinpointing amino acids crucial for barnase activity. Furthermore, by replacing K108N/I109R in barnase 20 with K108A/I109A (creating variant #21), we observed an increase in activity, indicating the significance of specific amino acid substitutions in barnase engineering. To further expand our library of barnase variants, we generated an additional nineteen variants, including those with either N- or C-terminal truncations, as well as combinations of truncations and mutations (#22 to #40, Supplementary Data 1). Among these, two variants (#38 and #39), featuring 20-amino acid N-terminal truncations and specific substitutions at position K108N and Q104K/K108N, respectively, displayed reduced off-target cleavage while exhibiting slightly weaker on-target activities compared to barnase 11 (Fig. 1c, pink zone). Given the significance of the peptide linker in constructing bioactive fusion proteins[38], we replaced the $(GGS)_3$ linker in a series of d*Ec*Cas6-barnase variants displaying a range of activities with two alternative linkers: a hemagglutinin (HA) tag sequence (YPYDVPDYA) and a longer $(GGS)_6$ linker. We observed that different linkers distinctly influenced barnase activity levels (Supplementary Fig. 2). Specifically, barnase 18 (K27A/N58D/R59A/E73A/K108N/I109R) with HA linker (hereafter referred to as #41) showed enhanced on-target cleavage but increased off-target activity compared to barnase 11. Altogether, we identified four barnase variants (#11, #38, #39, and #41) with optimal activities through the comprehensive mutagenesis and linker replacement studies.

Next, we expanded our study to include two additional type II toxins, MqsR and MaZF, known for their specific RNA cleavage motifs, ˆGˆC and AˆCA[24,36,39], respectively. As shown in Fig. 1b, for wild-type MqsR (wtMqsR), the two catalytic residues (K55 and Y80) and six residues (H6, S26, K55, R71, L81, and K97) are essential for RNA cleavage and substrate RNA binding, respectively. For wild-type MaZF (wtMaZF), five residues (Q24, R28, T51, T52, and Q53) are critical for RNA cleavage, while two residues (W13 and P29) are important for substrate RNA binding. Using an approach similar to that employed with barnase, we engineered 23 variants for d*Ec*Cas6-MqsR (referred to as #1 to #23, Fig. 1d, orange zone) and thirteen variants for d*Ec*Cas6-MaZF (referred to as #1 to #13, Supplementary Fig. 3), all incorporating a NES and a $(GGS)_3$ linker. Unlike wtbarnase, we acquired both wtMqsR and wtMaZF, which exhibited reduced toxicity to *E. coli* DH5α host cells, likely due to their more stringent cleavage motifs compared to the broader motif (GˆN) of wtbarnase. Using the dual-fluorescence reporter system, we observed that MqsR 20 (Y60A/K97A) exhibited minimal off-target cleavage while maintaining robust on-target activity. However, none of MaZF variants exhibited optimal activities. We then generated an additional eight MqsR variants (#24 to #31) and seventeen MaZF variants (#14 to #30). Among these, MqsR 29 (H6A/M57A/K97A) and MaZF 21 (R28S/I80A) and 28 (S54A/K55A/G56A/Y57A) showed optimal activity (Supplementary Fig. 4 and Fig. 1d, green zone). Together with the four previously identified d*Ec*Cas6-barnase variants, we proceeded to evaluate the cell toxicity of these eight d*Ec*Cas6-toxin fusions using a CCK-8 assay 48 hours post-transfection. We observed that all eight high-performing variants (pink columns) displayed minimal toxicities, whereas their high-activity counterparts (brown columns) showed obvious toxicity (Fig. 1e). In summary, based on both off-target and on-target cleavage activities, we ranked the performances of the eight screened d*Ec*Cas6-toxins as follows: d*Ec*Cas6-barnase 11 was the most effective, followed by d*Ec*Cas6-MaZF 28, d*Ec*Cas6-MqsR 20, d*Ec*Cas6-MaZF 21, d*Ec*Cas6-MqsR 29, d*Ec*Cas6-barnase 39, d*Ec*Cas6-barnase 38, and d*Ec*Cas6-barnase 41 (Supplementary Data 2).

Characterization of CBS features for *Ec*Cas6 cleavage

To elucidate the essential feature of the CBS sequence governing *Ec*Cas6 cleavage, we divided the 29-nt wtCBS into four distinct regions: a stem (6 base-pairs (bp)), a loop (4 nt), a 5′ flanking sequence (5 nt), and a 3′ flanking sequence (8 nt) (Fig. 2a). We engineered a series of CBS variants (enCBS) by introducing alterations in sequence and structure within these regions and integrated them into the 5′ UTR of GFP mRNA to fabricate a GFP-OFF reporter system (enCBS-GFP-OFF reporter), which was designed to reduce fluorescence upon *Ec*Cas6 recognition and cleavage (Fig. 2b). We co-transfected enCBS-GFP-OFF reporter plasmids and *Ec*Cas6-coding plasmids into HEK293T cells, and measured GFP expression levels 48 h post-transfection. As shown in Fig. 2c, 1-bp and 2-bp stem truncations at either the top (t-1, t-2) or bottom (b-1, b-2) resulted in *Ec*Cas6 nuclease activities comparable to or slightly lower than that of wtCBS. However, a 3-bp stem truncation at either end (t-3, b-3) nearly eliminated nuclease activity. Extension of the stem with random sequences with varying lengths (4, 14, and 24 bp) at the top (t + 4 R, t + 14 R, t + 24 R) or with four C-G base pairs at the bottom (b + 4CG) maintained *Ec*Cas6 activities similar to wtCBS. In contrast, the bottom of stem could not tolerate extensions of random base pairs (b + 4 R). Interestingly, enCBS (t-2), which features a single base-pair change (C-G to G-C), outperformed enCBS (b-2). Based on these findings, we selected enCBS (t-2) with a 4-bp stem as a model to further investigate the effects of G-C base-pair substitutions within the stem (Supplementary Fig. 5). Substitutions in the vicinity of the loop region (C9G, C8G, C9U, C8U, C9A) yielded cleavage activities comparable to or slightly lower than wtCBS. However, alterations closer to the flanking regions significantly reduced activities, and multiple base-pair substitutions within these four C-G base pairs dramatically diminished activity, indicating the critical conservation of these C-G base-pairs within the stem.

Subsequently, we investigated the characteristics of the 4-nt loop region by creating enCBS variants with single or multiple mutations within the loop, observing no impact on *Ec*Cas6 cleavage activity (Supplementary Fig. 6). We further assessed the impact of varying loop size from 0 to 50 nt across three different stem lengths (4, 6, and 10 bp) in the high-performing enCBS variants (enCBS (t-2), wtCBS, and enCBS (t + 4 R)) identified in Fig. 2c. As shown in Fig. 2d, the loop region displayed high adaptability; however, enCBS variants with four base-pair stems, which could not support loops larger than 20 nt due to unfavorable thermodynamic stability. Additionally, the deletion of the 4 nt-loop in enCBS (t-2) resulted in the loss of cleavage activity (indicated by red arrows), likely due to the formation of incorrected hairpin structures predicted by thermodynamic simulations using the NUPACK software. In contrast, the deletion of the 4 nt-loop in wtCBS, and enCBS (t + 4 R) (indicated by red arrows), retained cleavage activity comparable to wtCBS, as these variants adopted structures similar to those of enCBS (t-2) and enCBS (t + 2 R) variants (Supplementary Fig. 7). Additionally, we observed that single nucleotide mutations within the 5′ and 3′ flanking sequences had minimal impact

https://doi.org/10.1038/s41467-025-63166-y

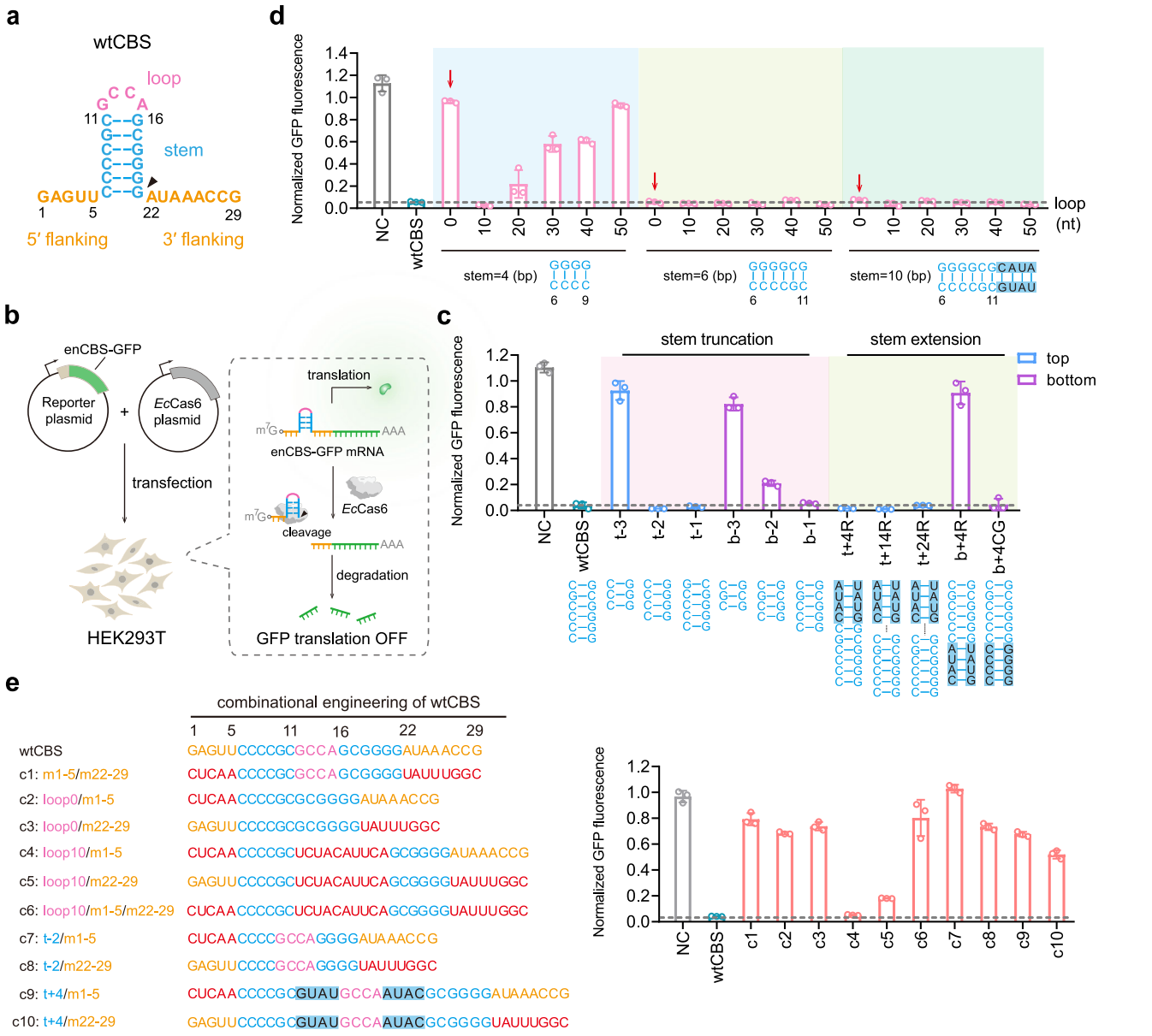

Fig. 2 | Investigation of CBS features for *Ec*Cas6 cleavage. a Schematic of four distinct regions of wtCBS, with numbered bases. The cleavage site (marked by a black triangle) indicates the GA junction between the stem and the 3′ flanking sequence cleaved by *Ec*Cas6. **b** Schematic of the enCBS-GFP-OFF reporter system, designed to assess the functionality of various CBS sequences in response to *Ec*Cas6 cleavage activity. **c** Investigation of the impact of stem truncation and extension of CBS on *Ec*Cas6 cleavage activity. **d** Investigation of the impact of the loop size of CBS with varying stem lengths on *Ec*Cas6 cleavage activity. **e** Investigation of the impact of combination engineering in the four regions of the wtCBS on *Ec*Cas6 cleavage activity. Negative control (NC) represents the GFP reporter plasmid without enCBS. GFP fluorescence values are normalized to the d*Ec*Cas6 control. Details of the tested enCBS variants are available in Supplementary Data 3. Data are mean ± s.e.m. of $n = 3$ biological replicates. Source data are provided as a Source data file.

on *Ec*Cas6 cleavage activity, and complete alterations of 3′ flanking sequences only slightly reduced activity (Supplementary Fig. 8). Finally, we performed a combinational engineering across the four distinct regions of the CBS, observing varying degrees of abolishment of *Ec*Cas6 cleavage compared to single-region modifications (Fig. 2e). Notably, the enCBS (c4, loop10/m1-5) maintained cleavage activity similar to wtCBS. Collectively, these findings elucidated the sequence and structure features of the CBS that are crucial for regulating *Ec*Cas6 activity and suggested the potential programmability of the CBS.

Characterization of CBS features for *Ec*Cas6 and d*Ec*Cas6 binding

To explore whether CBS features governing *Ec*Cas6 binding align with those required for *Ec*Cas6 cleavage, we devised a CRISPR activation (CRISPRa) system (Fig. 3a). This system comprises three components: a plasmid expressing nuclease-dead Cas9 from *Streptococcus pyogenes* (d*Spy*Cas9) along with sgRNA containing enCBS at its 3′ end (sgRNA-enCBS), a plasmid expressing *Ec*Cas6 fused with a transcriptional-activator VPR (*Ec*Cas6-VPR), and a plasmid containing the GFP gene under a minimal cytomegalovirus (miniCMV) promoter. The d*Spy*-Cas9/sgRNA-enCBS complex is designed to target the upstream region of the miniCMV promoter without initiating transcription of the downstream GFP gene. Subsequent recruitment of *Ec*Cas6-VPR to this complex activates GFP transcription, with binding affinity directly correlating with GFP expression levels. We tested six distinct CBS constructs (wtCBS, m1-5, t-2, t + 4CG, loop10, and m22-29), all of which were cleavable by *Ec*Cas6. We also included a variant with a deletion in the 3′ flanking region (referred to as d22-29), mimicking the *Ec*Cas6

https://doi.org/10.1038/s41467-025-63166-y

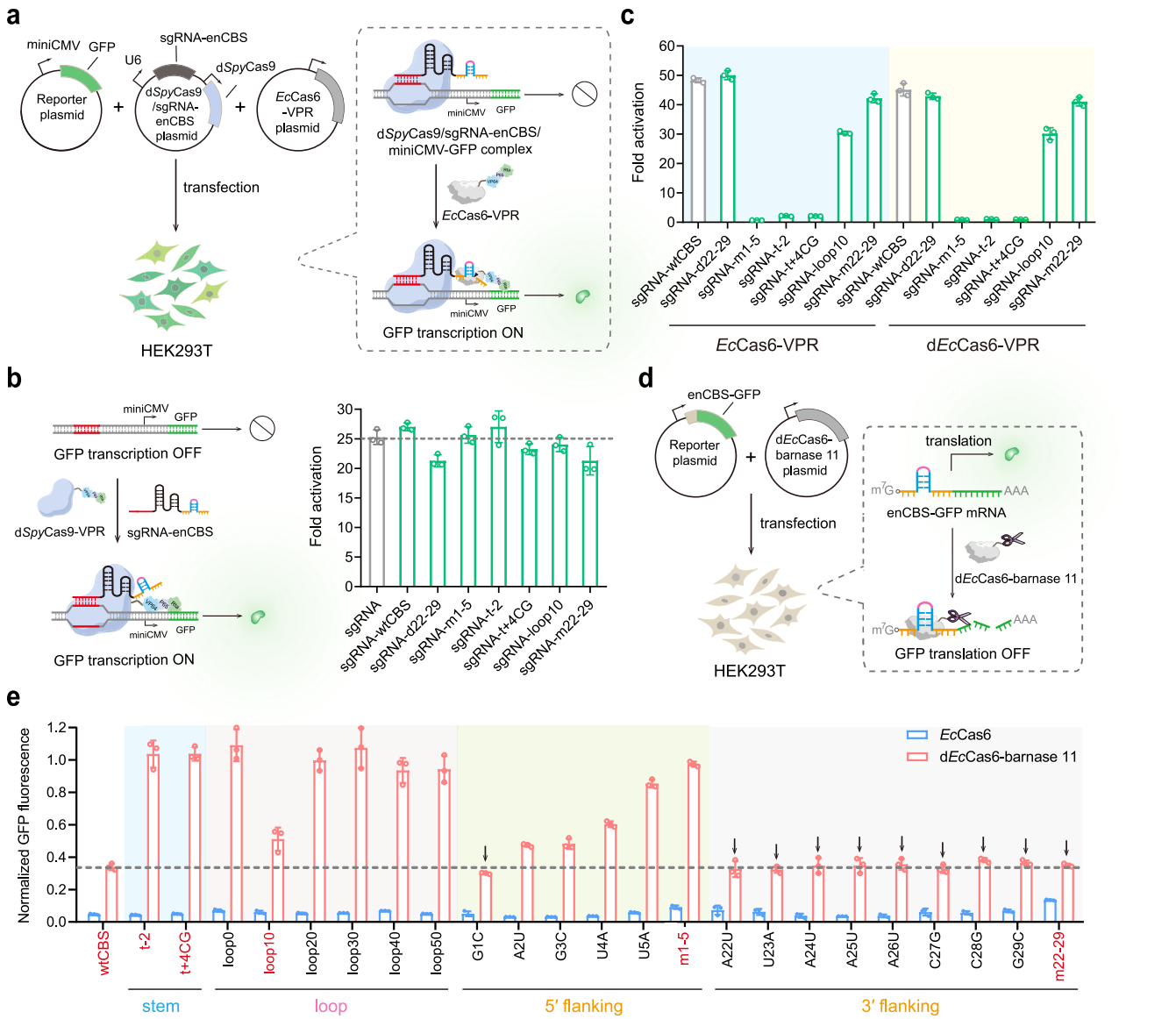

Fig. 3 | Investigation of CBS features for *Ec*Cas6 and d*Ec*Cas6 binding. **a** Schematic of the *Ec*Cas6-VPR-based CRISPRa reporter system in response to *Ec*Cas6 binding affinity. **b** Left: Schematic of the d*Spy*Cas9-VPR-based CRISPRa system with sgRNA-enCBS. Right: Fold increase in fluorescence for the seven sgRNA-enCBS variants and sgRNA in the d*Spy*Cas9-VPR-based CRISPRa system, compared with the control expressing d*Spy*Cas9-VPR and non-targeting sgRNA. **c** Fold increase in fluorescence for the seven sgRNA-enCBS variants induced by *Ec*Cas6-VPR or d*Ec*Cas6-VPR, compared with the control expressing d*Spy*Cas9, non-targeting sgRNA-wtCBS, and *Ec*Cas6-VPR or d*Ec*Cas6-VPR. **d** Schematic of the working principle of the enCBS-GFP-OFF reporter system using d*Ec*Cas6-barnase 11. **e** Comparison of the degradation efficiency of a panel of enCBS-GFP mRNAs, induced by d*Ec*Cas6-barnase 11 and *Ec*Cas6. GFP fluorescence values are normalized to the d*Ec*Cas6 control. Data are mean ± s.e.m. of $n = 3$ biological replicates. Source data are provided as a Source data file.

cleavage product and known for high binding affinity[28]. To confirm that the attachment of enCBS to sgRNAs did not interfere with d*Spy*Cas9 targeting and binding, we fused VPR to the d*Spy*Cas9 and measured GFP levels using sgRNA-enCBS (Fig. 3b, left). No significant differences were observed in GFP activation efficiency between the tested sgRNA-enCBS variants and the standard sgRNA (Fig. 3b, right). In contrast, these constructs exhibited varying levels of GFP expression (Fig. 3c, blue zone), indicating different binding affinities to *Ec*Cas6. The m22-29 and d22-29 demonstrated similar affinities to the wtCBS, while loop10 exhibited reduced binding. Constructs m1-5, t-2, and t + 4CG showed notably low affinity. These results suggested that specific CBS structural features are critical for stable *Ec*Cas6 binding.

Furthermore, we utilized the d*Ec*Cas6-VPR-based CRISPRa system to assess the binding affinities of enCBS variants to d*Ec*Cas6. As expected, the observed binding affinities were consistent with those of the enCBS variants to *Ec*Cas6 (Fig. 3c, yellow zone). In our design, we hypothesized that a stable complex formation between d*Ec*Cas6-toxin and CBS would enhance the efficacy of the toxin on RNA substrates. To test this, we employed the established enCBS-GFP-OFF system, which is designed to reduce GFP expression upon d*Ec*Cas6-barnase 11 binding and subsequent cleavage of enCBS-GFP mRNA in HEK293T cells (Fig. 3d). We selected a series of enCBS variants, previously identified as effective substrates for *Ec*Cas6 cleavage, to evaluate their binding affinities to d*Ec*Cas6. For a direct comparison, we measured the cleavage efficiency of d*Ec*Cas6-barnase 11 relative to *Ec*Cas6 on the enCBS-GFP mRNA (Fig. 3e). We observed that enCBS variants with the first base mutation in the 5′ flanking region (G1C) and substitutions in the 3′ flanking region (single and multiple mutations) displayed nuclease activity (indicated by black arrows) comparable to that of wtCBS. However, other enCBS variants tested, such as those with altered stem

https://doi.org/10.1038/s41467-025-63166-y

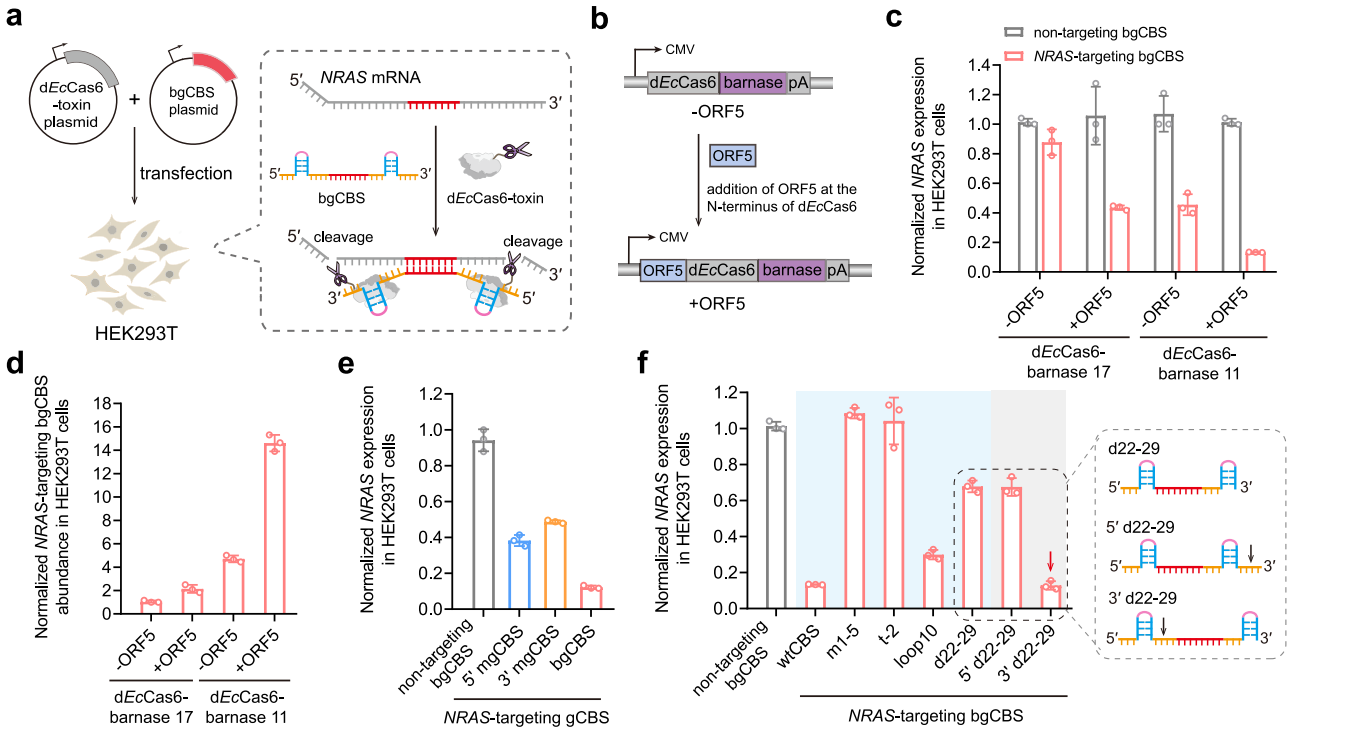

Fig. 4 | Rational design of guide CBS in STAR. a Schematic of working principle of STAR for *NRAS* transcript degradation in HEK293T cells. **b** Diagram showing the design of d*Ec*Cas6-barnase fusion coupled with the ssRNA-binding protein ORF5. **c** Evaluation of knockdown efficiency of d*Ec*Cas6-barnase 17 and d*Ec*Cas6-barnase 11 with or without the ORF5 at the N terminus. bgCBS utilized either a random 40-nt spacer sequence (referred to as non-targeting) or a 40-nt targeting spacer sequence. **d** Analysis of *NRAS*-targeting bgCBS abundances in HEK293T cells transfected with either d*Ec*Cas6-barnase 17 or d*Ec*Cas6-barnase 11, with or without ORF5. Data are normalized to the group transfected with *NRAS*-targeting bgCBS and d*Ec*Cas6-barnase 17. **e** Evaluation of *NRAS* transcript knockdown efficiency using mgCBS constructs with wtCBS at the 5′ end (5′ mgCBS) or the 3′ end (3′ mgCBS), and bgCBS containing wtCBS. **f** Knockdown efficiency of *NRAS* transcript using bgCBS constructs incorporating enCBS variants with varying affinities to d*Ec*Cas6. bgCBS constructs were prepared using enCBS (m1-5), enCBS (t-2), enCBS (loop10), and enCBS (d22-29), with results normalized to the non-targeting bgCBS. Heterozygous bgCBS constructs were prepared with enCBS (d22-29) at the 5′ end (5′ d22-29) or at the 3′ end (3′ d22-29), and wtCBS at the opposite end. The black arrows indicate the 8-nt 3′ flanking. The red lines represent the spacers in bgCBS constructs. Data are mean ± s.e.m. of $n = 3$ biological replicates. Source data are provided as a Source data file.

lengths of 4 and 10 bp, varied loop sizes from 0 to 50 nt, and mutations from the second to the fifth base in the 5′ flanking region, showed a pronounced reduction or a complete loss of degradation activity. These reduced activities reflected a lower binding affinity, leading to rapid dissociation of d*Ec*Cas6-barnase from these enCBS variants and thus impairing the RNA degradation mediated by barnase. The binding affinities of enCBS variants (denoted in red font on the X-axis, Fig. 3e), determined by the d*Ec*Cas6-barnase system, were consistent with those measured using the d*Ec*Cas6-VPR system. Together, these results suggested that stable d*Ec*Cas6 binding requires stricter sequence requirements than *Ec*Cas6 cleavage.

Design of guide CBS in STAR

To pilot the STAR concept, we initially designed a bivalent guide CBS (bgCBS) by combining two wtCBS with a spacer complementary to the *NRAS* transcript, enabling the recruitment of d*Ec*Cas6-toxin in HEK293T cells (Fig. 4a). Referring to the CIRTS design[23], we appended a non-specific viral ssRNA-binding protein, ORF5, to the N-terminus of d*Ec*Cas6-barnase (Fig. 4b). We co-transfected two active forms of d*Ec*Cas6-barnase, d*Ec*Cas6-barnase 17 and d*Ec*Cas6-barnase 11, either alone or in tandem with ORF5, alongside bgCBS constructs featuring 40-nt targeting spacers that contained nine GN sites (Supplementary Fig. 9). As shown in Fig. 4c, in the absence of ORF5, the high-activity d*Ec*Cas6-barnase 17 induced minimal *NRAS* degradation, while the low-activity d*Ec*Cas6-barnase 11 reduced *NRAS* levels by 55%. Incorporating ORF5 with both d*Ec*Cas6-barnase variants significantly increased the knockdown efficiency, with the ORF5-d*Ec*Cas6-barnase 11 achieving an impressive 87% reduction in *NRAS* levels. We hypothesized that the reduced effectiveness of the high-activity d*Ec*Cas6-barnase 17 might be attributed to its greater tendency to degrade the spacer before the targeting process, compared to the low-activity d*Ec*Cas6-barnase 11. The presence of ORF5 likely shielded the spacer from barnase degradation, preserving it for targeting process and enhancing degradation efficiency. To test this, we measured *NRAS*-targeting bgCBS levels in the presence and absence of ORF5 using both d*Ec*Cas6-barnase 17 and d*Ec*Cas6-barnase 11. The results showed that the abundance of *NRAS*-targeting bgCBS was significantly higher when ORF5 was added to d*Ec*Cas6-barnase (Fig. 4d), confirming that ORF5 substantially stabilized bgCBS, which correlated with improved target degradation efficiency. These findings suggested the critical role of spacer protection in optimizing the performance of the STAR system.

Next, we investigated the impact of spacer length on degradation efficiency by co-expressing ORF5-d*Ec*Cas6-barnase 11 with bgCBS constructs of varying spacer lengths (20, 30, 40, and 50 nt) (Supplementary Fig. 10). We observed a progressive increase in efficiency with longer spacers, with bgCBS constructs containing 40- and 50-nt spacers achieving the highest knockdown of *NRAS* transcript levels. Notably, transfection of the targeting bgCBS constructs with a 40-nt spacer alone (without ORF5-d*Ec*Cas6-barnase 11) did not induce *NRAS* knockdown (Supplementary Fig. 11a), ruling out RNAi as the degradation mechanism. Additionally, co-transfection of plasmids expressing d*Ec*Cas6 and targeting bgCBS had no effect on *NRAS* transcript

levels (Supplementary Fig. 11b), further confirming that the observed degradation was specifically mediated by barnase. Furthermore, we tested two monovalent gCBS (mgCBS) constructs, each containing a single wtCBS flanked by a 40-nt spacer at either the 5′ or 3′ end. These mgCBS constructs achieved knockdown efficiencies of 60% and 50%, respectively, which were lower than that achieved with the bgCBS construct (Fig. 4e). We speculated that bivalent design of the bgCBS constructs enhances the stability of the gCBS construct and facilitates recruitment of two ORF5-d*Ec*Cas6-barnase 11 molecules per target, thereby enhancing the overall degradation efficiency. Optimization of transfection conditions revealed that a 200-ng dose of ORF5-d*Ec*Cas6-barnase 11 plasmid combined with 400 ng of bgCBS plasmid yielded optimal knockdown (Supplementary Fig. 12). To assess the knockdown kinetics, we monitored *NRAS* transcript levels over a 5-day time course. The maximum reduction occurred 2 days post-transfection and gradually declined thereafter (Supplementary Fig. 13), consistent with the transient nature of plasmid delivery[10].

Finally, we investigated the effect of d*Ec*Cas6 binding affinity to CBS on knockdown levels by introducing enCBS variants with distinct binding affinities into the bgCBS architecture. Four enCBS variants, including m1-5, t-2, loop10, and d22-29, were selected to fabricate bgCBS constructs (Supplementary Fig. 14). As shown in the blue zone of Fig. 4f, enCBS (m1-5) and enCBS (t-2) with low binding affinities resulted in a complete loss of knockdown efficacy. The enCBS (loop 10), which displayed a slightly lower affinity than wtCBS, retained partial but diminished knockdown efficiency. Unexpectedly, the high-affinity enCBS (d22-29) failed to match wtCBS-level knockdown. To elucidate this result, we assessed positional effects of enCBS (d22-29) in mgCBS constructs (Supplementary Fig. 15) and heterozygous bgCBS constructs (Fig. 4f, gray zone), using wtCBS as a control. In mgCBS constructs, d22-29 positioned at the 5′ end reduced *NRAS* knockdown to 25%, significantly lower than that of its wtCBS counterpart at the same position. In contrast, placing enCBS (d22-29) at the 3′ end restored efficiency comparable to the 3′ wtCBS. In the heterozygous bgCBS construct, pairing enCBS (d22-29) at the 3′ end with wtCBS at the 5′ end produced bgCBS (wtCBS)-level knockdown (87%), while the reverse configuration of enCBS (d22-29) at the 5′ end caused a 33% reduction. These disparities may arise from steric constraints caused by the rigid binding of ORF5-d*Ec*Cas6-barnase 11 to the high-affinity d22-29, which impedes spacer-target interaction at the 5′ end. In contrast, the 8-nt 3′ flanking sequence provides sufficient spatial flexibility, allowing the 40-nt spacer to engage the target. Given its wtCBS-matching efficacy, we adopted this shorter heterozygous bgCBS design (3′ d22-29) for subsequent experiments.

Endogenous RNA degradation by STAR

Following the development of the gCBS design, we assessed the knockdown efficacy of STAR using the above eight engineered d*Ec*Cas6-toxins, each fused to ORF5 at the N terminus of d*Ec*Cas6 and targeting the *NRAS* transcript. For comparison, we included the reported *Rfx*Cas13d[40] and shRNA[41] knockdown methods, optimized to their respective transfection doses (Supplementary Fig. 16). Among the d*Ec*Cas6-toxins, ORF5-d*Ec*Cas6-barnase 11, ORF5-d*Ec*Cas6-MqsR 20, and ORF5-d*Ec*Cas6-MaZF 28, achieved remarkable *NRAS* knockdown efficiencies of 87%, 91%, and 94%, respectively, surpassing both *Rfx*Cas13d and shRNA methods (Fig. 5a). Notably, ORF5-d*Ec*Cas6-barnase 11 with the flexible $(GGS)_3$ linker outperformed ORF5-d*Ec*Cas6-barnase 41 with the HA linker (35%). Moreover, we noticed that the 40-nt spacer contained only two MqsR and one MaZF cleavage sites (Supplementary Fig. 9), compared to the nine potential sites for barnase. This disparity prompted us to test the performance of d*Ec*Cas6-MqsR and d*Ec*Cas6-MaZF in the absence of the ORF5. As shown in Fig. 5b, d*Ec*Cas6-MqsR 20 and d*Ec*Cas6-MaZF 28 showed a slight decrease in knockdown efficiency to 82% and 90%, respectively, whereas their wild-type counterparts (d*Ec*Cas6-wtMqsR and d*Ec*Cas6-wtMaZF) lost nearly all activity. Restoration of function upon ORF5 fusion demonstrated its protective effect against bgCBS degradation when using highly active wtMqsR and wtMaZF. These results indicated that the engineered MqsR 20 and MaZF 28 enabled efficient RNA degradation without fusion to the ssRNA-binding protein due to their stringent cleavage motifs and reduced endoribonuclease activity. For MqsR and MaZF, we modified spacer sequences by replacing the GC and ACA with GU and GCA (Fig. 5c, left), eliminating toxin cleavage sites while preserving target transcript complementarity (GU wobble base pair). bgCBS constructs incorporating these redesigned spacers achieved *NRAS* knockdown efficiencies comparable to the original bgCBS (Fig. 5c, right). Based on these findings, we did not prioritize this strategy in the subsequent spacer design.

Next, we assessed the efficacy of STAR using ORF5-d*Ec*Cas6-barnase 11, d*Ec*Cas6-MqsR 20, and d*Ec*Cas6-MaZF 28 to degrade five cytoplasmic mRNAs: *PPIB*, *NFKB1*, *KRAS, SMAD4*, and *MYC*. For each target, we screened three potential binding sites and used ORF5-d*Ec*Cas6-barnase 11 to identify the optimal spacer (Supplementary Fig. 17). The observed variability in degradation efficiency among sites likely arose from differences in mRNA accessibility. The optimal spacers identified contained 4-19 GN motifs for barnase, 2-4 GC motifs for MqsR, and 0-1 ACA motif for MaZF (Supplementary Data 5). Across all transcripts, ORF5-d*Ec*Cas6-barnase 11, d*Ec*Cas6-MqsR 20, and d*Ec*Cas6-MaZF 28 achieved degradation efficiencies ranging from 61% to 78%, 60% to 77%, and 56% to 85%, respectively, matching or exceeding the performance of *Rfx*Cas13d and shRNA methods (Fig. 5d). We further evaluated the capacity of STAR to target nuclear ncRNAs, including *XIST* and *NEAT1*, each tested at two distinct sites. ORF5-d*Ec*Cas6-barnase 11 achieved 72% and 73% degradation of *XIST* and *NEAT1*, respectively. Similarly, d*Ec*Cas6-MqsR 20 resulted in 63% and 49%, while d*Ec*Cas6-MaZF 28 showed 63% and 54% degradation for the same targets (Fig. 5e and Supplementary Fig. 18). These results demonstrated a key advantage of STAR over RNAi-based approaches, as conventional RNAi is ineffective for nuclear ncRNAs due to its reliance on cytoplasmic degradation machinery. Notably, these high efficiencies were obtained without the enrichment of the transfected positive cells.

To evaluate the off-target effects, we conducted RNA sequencing in HEK293T cells to compare the specificity of the three high-efficiency STAR systems with *Rfx*Cas13d and shRNA methods. As shown in Fig. 5f, volcano plots of transcript levels from samples treated with the three STAR systems, alongside targeting and non-targeting controls, revealed varying impact on other transcripts. Notably, d*Ec*Cas6-MaZF 28 effectively depleted the *PPIB* transcript while showing minimal impact on other transcripts, with fewer than 100 genes downregulated and upregulated. In contrast, the *Rfx*Cas13d and shRNA methods resulted in a higher number of differentially expressed genes following *PPIB* knockdown, with hundreds of genes downregulated and upregulated, respectively. Collectively, these results demonstrated the robustness of STAR in achieving high-efficiency knockdown of endogenous transcripts with minimal off-target effects, validating its potential as an effective and reliable tool for RNA degradation.

Multiplex RNA knockdown activity of STAR via AAV delivery

The ability to perform multiplex knockdown is essential as it enables the concurrent silencing of several transcripts, which is crucial for deepening our understanding of complex biological processes and for advancing gene therapy. Before using AAV delivery, we validated the multiplexed knockdown capacity of STAR via plasmid delivery using the optimal d*Ec*Cas6-MaZF 28 as a model. We utilized individual U6 promoters to drive the expression of two or three bgCBS constructs, each targeting different gene combinations (Supplementary Fig. 19a). As shown in Supplementary Fig. 19b, when targeting two genes simultaneously, we achieved knockdown efficiencies of 83% and 81% for the targeted *NRAS* and *PPIB*, 87% and 76% for *NRAS* and *SMAD4*, and

https://doi.org/10.1038/s41467-025-63166-y

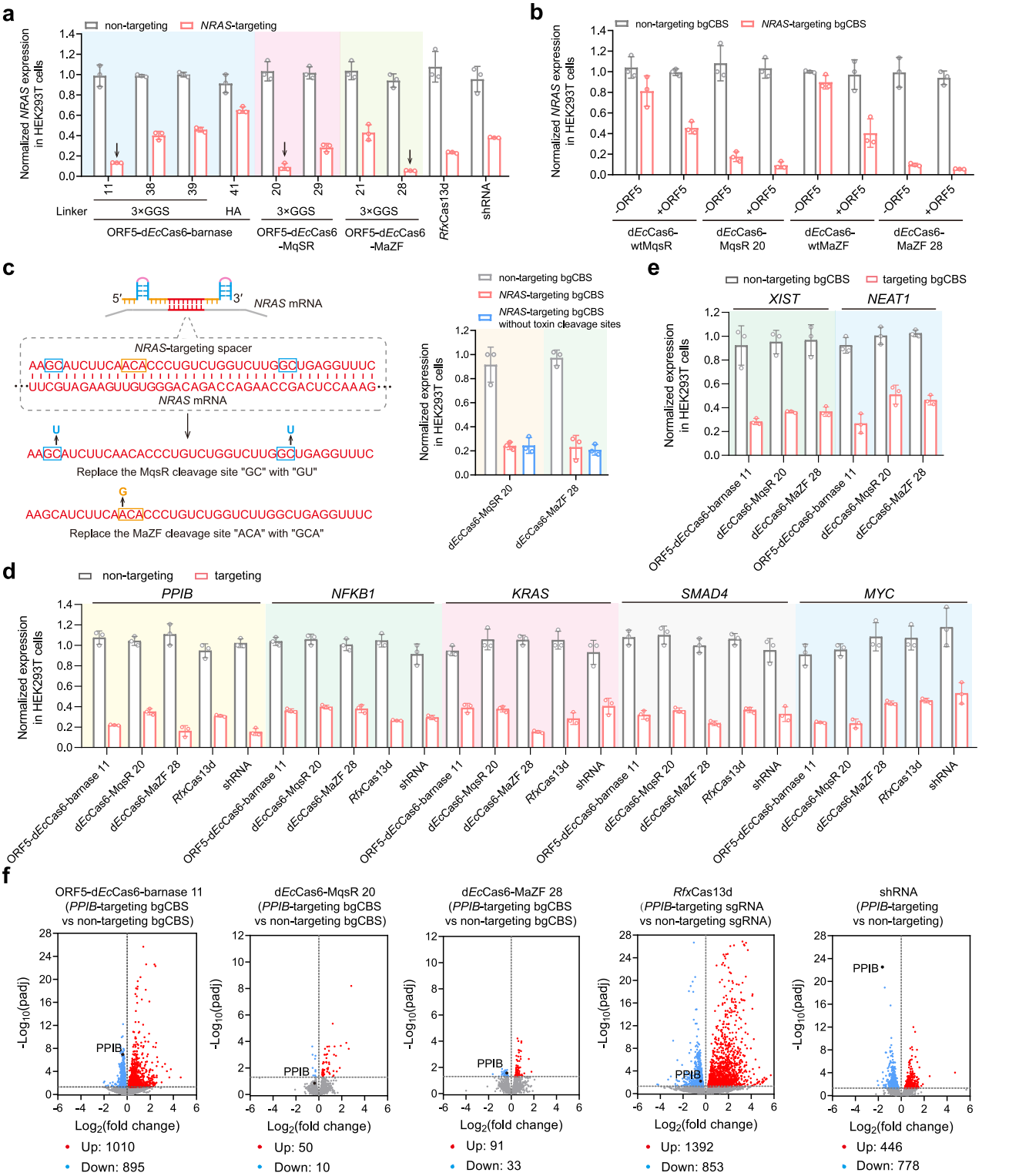

Fig. 5 | Knockdown of endogenous transcripts in mammalian cells by STAR. **a** Comparison of knockdown activity of eight selected ORF5-d*Ec*Ca6-toxins against *NRAS* transcript, alongside *Rfx*Cas13d and shRNA. **b** Comparison of the degradation efficiency of *NRAS* transcript using d*Ec*Cas6-wtMqsR, d*Ec*Cas6-MqsR 20, d*Ec*Cas6-wtMaZF, and d*Ec*Cas6-MaZF 28 with or without the ORF5 at the N terminus. **c** Investigation of *NRAS* knockdown efficiency using bgCBS incorporating the GU wobble base pair strategy for d*Ec*Cas6-MqsR 20 and d*Ec*Cas6-MaZF 28. Results are normalized to a non-targeting control. The blue frames represent the cleavage sequences of MqsR, while the orange frames represent the cleavage sequences of MaZF. **d** Comparison of knockdown efficiency of ORF5-d*Ec*Cas6-barnase 11, d*Ec*-Cas6-MqsR 20, d*Ec*Cas6-MaZF 28, *Rfx*Cas13d, and shRNA against five cytoplasmic mRNAs. Results are normalized to a non-targeting control. **e** Knockdown efficiency of ORF5-d*Ec*Cas6-barnase 11, d*Ec*Cas6-MqsR 20, and d*Ec*Cas6-MaZF 28 against two nuclear ncRNAs. Results are normalized to a non-targeting control. **f** Volcano plots showing differential transcript levels between HEK293T cells transfected with plasmids expressing ORF5-d*Ec*Cas6-barnase 11, d*Ec*Cas6-MqsR 20, d*Ec*Cas6-MaZF 28, *Rfx*Cas13d or shRNA, targeting *PPIB* versus a non-targeting control. Down-regulated transcripts are indicated in blue, while up-regulated transcripts are indicated in red. Benjamini-Hochberg correction for multiple testing was used after the Wald test. Data are mean ± s.e.m. of $n = 3$ biological replicates. Source data are provided as a Source data file.

https://doi.org/10.1038/s41467-025-63166-y

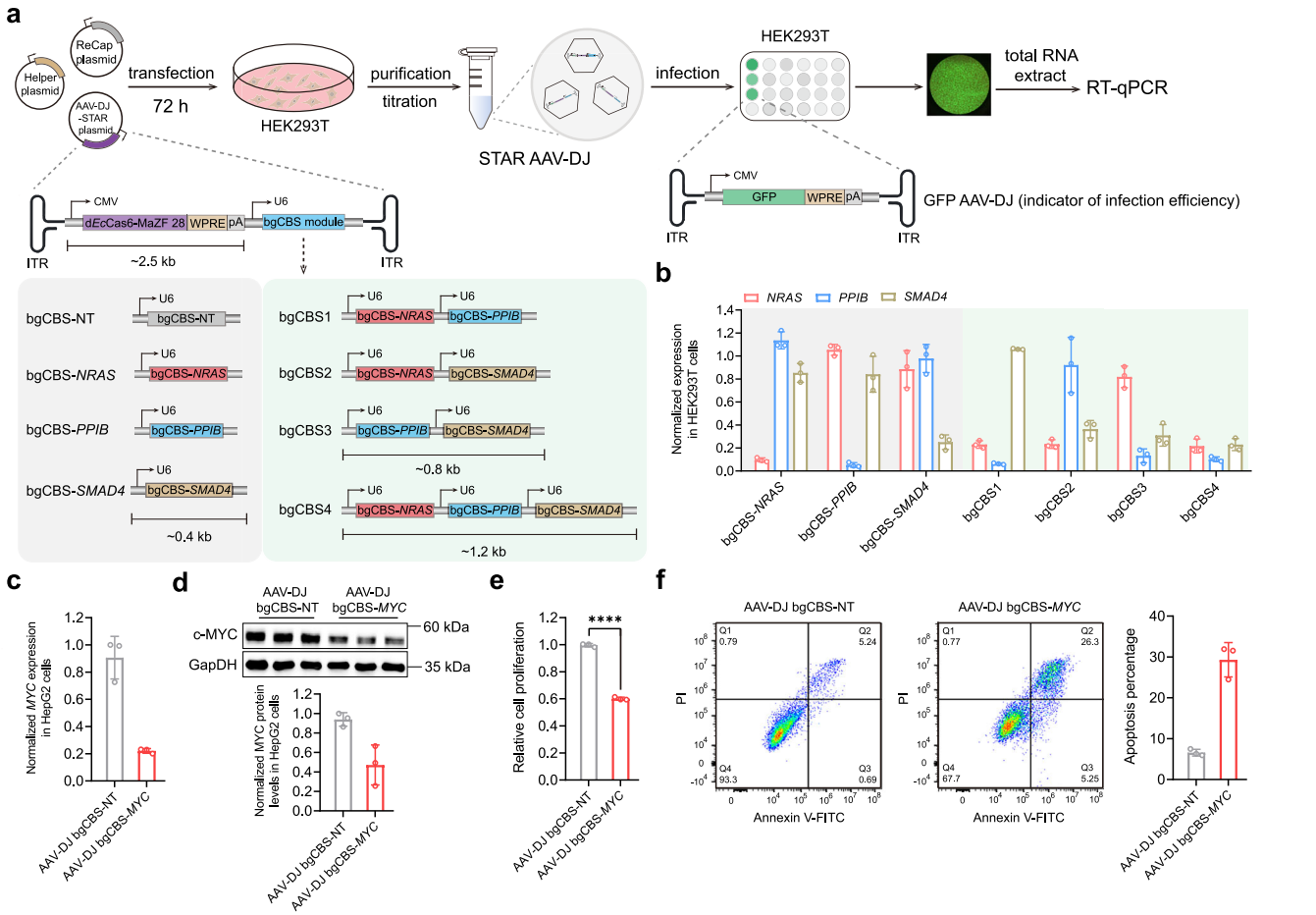

Fig. 6 | Validation of RNA knockdown activity of STAR via AAV delivery. **a** Schematic of the construction of STAR AAV-DJ for multiplex knockdown. **b** Comparative analysis of knockdown efficiency of STAR AAV-DJ on single and multiple RNA targets, normalized to the non-targeting STAR AAV-DJ. **c** Effect of STAR AAV-DJ on the knockdown of *MYC* mRNA in HepG2 cells, in contrast to a non-targeting control (AAV-DJ bgCBS-NT). **d** Effect of STAR AAV-DJ on MYC protein levels in HepG2 cells, relative to the non-targeting control. **e** Effect of STAR AAV-DJ on the proliferation of HepG2 cells. Significance determined by two-tailed Student's *t* test ($P < 0.0001$). ****$P < 0.0001$, *** $P < 0.001$, ** $P < 0.01$, * $P < 0.05$. **f** Induction of HepG2 cell apoptosis by STAR AAV-DJ, with representative flow cytometry data shown in the left panel and quantified apoptosis rates depicted in the right panel. Data are mean ± s.e.m. of $n = 3$ biological replicates. Source data are provided as a Source data file.

90% and 77% for *PPIB* and *SMAD4*. These efficiencies were comparable to those obtained with single bgCBS constructs. Slight reductions in efficiency were observed when targeting three gene simultaneously. Notably, there were no significant changes in the expression levels of non-targeted genes, confirming the high specificity of STAR.

AAV is a favored vector for clinical applications, offering numerous advantages such as low immunogenicity and pathogenicity, programmable tissue tropism, and high delivery efficiency[42]. Specifically, the AAV-DJ variant, which features a hybrid capsid derived from eight serotypes and demonstrates superior transduction efficiency compared to wild-type serotypes[43], was selected for delivering STAR. The hypercompact property of STAR fits within the 4.7 kb payload capacity, allowing for additional space to incorporate multiple bgCBS constructs for multiplexed RNA knockdown. We engineered the AAV-DJ vector to include similar bgCBS constructs as in plasmid delivery, and incorporated the coding sequence of d*Ec*Cas6-MaZF 28 under the control of a CMV promoter (Fig. 6a). These AAV-DJ particles were packaged, purified, and titrated. HEK293T cells were infected with AAV DJ-bgCBS *NRAS* at varying multiplicity of infection (MOI). We found that the optimal MOI for *NRAS* degradation was 1×10^5 vgs/cell (Supplementary Fig. 20a). Additionally, we repeated the plasmid-based *NRAS* knockdown kinetics experiment using AAV delivery. The knockdown peaked at 2 days post-infection and was maintained even at 5 days (Supplementary Fig. 20b), likely due to sustained retention and expression from the AAV vector. Next, we evaluated the multiplex knockdown capability. As shown in Fig. 6b, a single bgCBS in the AAV vector resulted in 90%, 95%, and 75% knockdown of *NRAS*, *PPIB*, and *SMAD4* transcripts, respectively. These efficiencies were slightly reduced when targeting multiple transcripts. Similar to plasmid delivery, AAV delivery did not significantly interfere with non-target transcripts. Collectively, these results clearly demonstrated the effectiveness of AAV-packaged STAR in degrading target transcripts.

Finally, we explored the potential therapeutic applications of STAR by targeting an oncogenic *MYC* mRNA. a significant yet challenging target due to the undruggable nature of the MYC oncoprotein, which plays a crucial role in both tumor initiation and maintenance and is deregulated in over 70% of human cancers[44,45]. We developed AAV-DJ particles carrying bgCBS designed to knockdown *MYC* mRNA in HepG2 cells. Two days post-infection, we assessed both *MYC* mRNA and protein levels. Our results demonstrated a significant reduction of up to 78% in *MYC* mRNA abundance (Fig. 6c), accompanied by a 53% decline in MYC protein levels (Fig. 6d). Moreover, the reduction in MYC protein levels were accompanied by a roughly 40% decrease in HepG2 cells proliferation (Fig. 6e). Additionally, we observed a 23% increase in HepG2 cell apoptosis, as indicated by a shift in the cell population in the flow cytometry analysis (Fig. 6f). These findings suggested the

potential of STAR to modulate cellular processes through targeted RNA knockdown, offering a promising avenue for therapeutic applications.

Discussion

In this study, we developed STAR, an hypercompact protein-based artificial transcript degrader, assembled de novo from engineered toxins integrated with the CRISPR effector d*Ec*Cas6 and its cognate CBS. A pivotal component of STAR is the sequence-specific toxin endoribonuclease, crafted to meet two critical criteria: first, it features a broad cleavage motif, ideally targeting fewer than four nucleotides, making it a versatile ribonuclease within the cellular milieu; second, it is engineered to minimize the degradation of non-target transcripts, a vital feature considering the prevalence of simple cleavage motifs in cells. To satisfy these stringent requirements, we systematically engineered three toxins, including barnase, MqsR, and MaZF, to attenuate their potent endonuclease activities. We fused engineered toxins with the d*Ec*Cas6-CBS system to convert them into targeting RNA ribonucleases. Transcript knockdown assays conducted via plasmid delivery identified three optimal degraders: ORF5-d*Ec*Cs6-barnase 11 (430 amino acids), d*Ec*Cas6-MqSR 20 (317 amino acids), and d*Ec*Cas6-MaZF 28 (330 amino acids), which achieved degradation efficiencies ranging from 61% to 87%, 60% to 82%, and 56% to 90%, respectively (Fig. 5a–c). This high performance was achieved without selective enrichment of transfected cells, matching and surpassing the efficacy of *Rfx*Cas13d and shRNA methods.

Our study also offers insights that broaden the understanding of the *Ec*Cas6-CBS system and its potential applications. We conducted a thorough characterization of the CBS features governing *Ec*Cas6 cleavage and binding, revealing distinct requirements for each. The sequence is conservative for stable *Ec*Cas6 and d*Ec*Cas6 binding but highly tuneable for *Ec*Cas6 cleavage, particularly with notable flexibility in the loop region (Figs. 2 and 3). These findings are pivotal for advancing technologies that rely on the precise cleavage capability of *Ec*Cas6. For instance, it is conceivable to incorporate specific RNA aptamers sensitive to various molecules within the loop region, to ingeniously design blocked CBS to regulate the cleavage activity of *Ec*Cas6 in a molecule-responsive and controlled manner through allosteric effects.

The use of non-specific ribonucleases in artificial RNA targeting systems raises concerns about potential degradation of the gRNA spacer before reaching its target site. To address this, the Pin-based CIRTS employs the ssRNA-binding protein ORF5 to protect the spacer, ensuring efficient target RNA degradation. Our study, however, revealed varying dependencies on ORF5 among three engineered toxins. For barnase, which has a simple GN cleavage motif, the ORF5 protein is crucial due to the numerous potential cleavage sites within the spacer. The inclusion of the ORF5 module enhanced degradation efficiency by 32% (Fig. 4c). In contrast, MqsR and MaZF, with more specific cleavage motifs, have fewer spacer cleavage sites, reducing the risk of spacer degradation. Our data showed that engineered MqsR and MaZF systems achieved high-efficiency RNA knockdown without ORF5 (Fig. 5b,d,e). Notably, for MqsR and MaZF, using GU wobble base pair strategy in the spacer avoided toxin cleavage site while maintaining target complementarity, which would be a promising strategy for spacer design to completely avoid potential spacer degradation. These findings simplify the STAR construct by eliminating the 108-amino-acid ORF5 element, minimizing potential cellular perturbations from exogenous ORF5.

A key advantage of STAR over RNAi lies in its ability to efficiently degrade nuclear transcripts (Fig. 5e), a challenge for RNAi due to its reliance on cytoplasmic machinery. Compared to naturally evolved CRISPR-Cas-based RNA knockdown systems, such as the CRISPR-Csm complex with over 2000 amino acids[10], Cas7-11 with 1602 amino acids[11], *Lsh*Cas13a from *Leptotrichia shahii* with 1389 amino acids[46], *Psp*Cas13b from *Prevotella sp. P5-125* with 1090 amino acids[47], and *Rfx*Cas13d with 956 amino acids[13], STAR features a significantly hypercompact size, ranging 317 to 430 amino acids. This hypercompact size greatly facilitates in vivo delivery and multiplex knockdown via AAV vectors. Moreover, STAR exhibits substantially lower off-target degradation compared to the *Rfx*Cas13d technology (Fig. 5f). These attributes, including its hypercompact size and markedly reduced off-target effects, position STAR as a competitive alternative to the widely used Cas13 family. Our toxin engineering strategy has yielded promising results, and the DH5α-assisted natural mutagenesis has enriched our toxin mutation library. However, there is considerable potential to explore a broader spectrum of mutants that achieve a better balance between off-target and on-target activities. This exploration could be advanced by refining the mutagenesis techniques, potentially through the use of protein-directed evolution technologies[48,49]. Overall, STAR has established a foundation for harnessing toxins to create hypercompact, efficient, and specific artificial RNA degraders. With continued improvements, STAR is well-positioned to make significant contributions to both fundamental research and clinical applications.

Methods

Plasmid construction

Primers used in this work were synthesis by Beijing Tsingke Biotech Co., Ltd (Tianjin, China), the gene fragments of *Ec*Cas6 and three toxins were synthesized by GenScript (Nanjing, China). The *Rfx*Cas13d plasmid and the shRNA vector were purchased from Miaoling Biotech Co., Ltd. *Ec*Cas6 and *Rfx*Cas13d fragments underwent PCR amplification using 2× Phanta UniFi Master Mix (Dye Plus) (P526, Vazyme Biotech Co., Ltd, Nanjing, China), then cloned into a pCMV vector via 2× MultiF Seamless Assembly Mix (RK21020, Abclonal Technology, Wuhan, China), and transformed into Trelief 5α chemically competent cell (DLC101, Beijing Tsingke Biotech Co., Ltd, Tianjin, China). To generate d*Ec*Cas6-toxin mutants, various toxin mutations were introduced via PCR and the amplification products were overlapped with the d*Ec*Cas6 fragment before being cloned into a pCMV vector. The amino acid sequences of mutants are listed in Supplementary Data 1. Similarly, for reporter plasmid constructs, the sequences of wtCBS or enCBS (Supplementary Data 3) were synthesized and overlapped with GFP coding sequence, and cloned into a pCMV vector containing BFP expression fragment. For the generation of bgCBS and sgRNA, their sequences were PCR-amplified with the sequence of U6 promotor and subsequently cloned into a pCMV vector. For shRNA plasmid constructs, the shRNA oligos were annealed and ligated into Age I and EcoR I sites of pLKO.1 vectors using T4 DNA ligase (FL101, TransGen Biotech Co., Ltd, Beijing, China). All the guide sequences used for targeting transcripts are listed in Supplementary Data 4. For AAV plasmid constructs, fragments encoding STAR were cloned into ITR sites of a AAV vector. All PCR products were purified using PCR Product Recovery kit (GK2045, Generay Biotech Co., Ltd, Shanghai, China), and plasmids were extracted using AFTSpin EndoFree Plasmid Mini kit (RK30102, Abclonal Technology, Wuhan, China), following the manufacturer's instructions. The bacteriological petri dishes, pipette tips, and tubes were purchased from Bioland Co., Ltd (Hangzhou, China).

Cell culture and transfection

HEK293T (SCSP-502) and HepG2 (SCSP-510) cells were obtained from the Cell Bank of Chinese Academy. All cell lines were cultured in 10 cm dishes containing 10 mL high-glucose Dulbecco's modified Eagle's medium (DMEM), supplemented with 10% (v/v) FBS (C04001, TransGen Biotech Co., Ltd, Beijing, China) and 1% (v/v) penicillin/streptomycin (P/S) at 37 °C in a humidified 5% CO_2 incubator. Cells were seeded on 24-well plates and allowed to reach approximately 60% confluency before transfection. For the high-performance d*Ec*Cas6-toxin variant screen assay, a dual fluorescence plasmid and d*Ec*Cas6-

toxin mutant plasmids (1:1 ratio; a total of 400 ng of plasmids) were mixed with 40 μL of Opti-MEM and 0.8 μL of Lipo8000™ transfection reagent (C0533, Beyotime Biotech Co., Ltd, Nantong, China). For the *Ec*Cas6 and d*Ec*Cas6-barnase 11 cleavage assay, *Ec*Cas6 or d*Ec*Cas6-barnase 11 plasmids were mixed with enCBS-GFP plasmid (1:1 ratio; a total of 400 ng of plasmids) combined with 40 μL of Opti-MEM and 0.8 μL of Lipo8000™. For the CRISPRa assay, 200 ng of miniCMV-GFP, 300 ng of d*Spy*Cas9/sgRNA-enCBS, and 300 ng of d*Ec*Cas6-VPR or *Ec*Cas6-VPR plasmids were mixed with 40 μL of Opti-MEM and 1.2 μL of Lipo8000™. For the RNA knockdown assay, 200 ng of d*Ec*Cas6-toxin and 400 ng of bgCBS plasmids, 300 ng of *Rfx*Cas13d and 400 ng of sgRNA plasmids, and 500 ng of shRNA plasmid were mixed with 40 μL of Opti-MEM and 1 μL of Lipo8000™, respectively. Transfection was then conducted according to the manufacturer's instructions. 48 h after transfection, cells were harvested for subsequent experiments.

Flow cytometry experiment

After the cells were transfected and cultured for 48 h, the medium was removed and resuspended in 500 μL of phosphate-buffered saline (PBS) followed by centrifuging at 4 °C for 5 min at 845 *g*. The supernatant was discarded and cells were resuspended in 300 μL of PBS. Cell fluorescence was measured using a Beckman flow cytometer equipped with a 488 nm excitation laser and a 530/30 emission filter for GFP, and a 450 nm excitation laser with a 520/15 emission filter for BFP. Fluorescence data were collected with CytExpert (v2.3). The normalized fluorescence was calculated as the fluorescence of d*Ec*Cas6-toxins or *Ec*Cas6 versus d*Ec*Cas6.

Extraction of total RNA and quantitative PCR

Total cell RNA was harvest using *SteadyPure* RNA Extraction kit (AG21024, Accurate Biotechnology (HUNAN) Co., Ltd, ChangSha, China) following the manufacturer's manuals. The concentration of total RNA was measured by a microplate reader (BioTek Instrument, Winooski, VT, USA). The extracted RNA was then converted to cDNA using ToloScript All-in-one RT EasyMix (22107, Tolo Biotech Co., Ltd, Shanghai, China) according to manufacturer's instructions. Briefly, a total volume of 20 μL containing total RNA (1 μg), 5× All-in-one RT buffer (4 μL), All-in-one Enzyme mix (1 μL), and RNase-free H_2O (to 20 μL) was incubated at 50 °C for 15 min and 85 °C for 5 s for reverse transcription. The bgCBS was converted to cDNA using miRNA First Strand cDNA Synthesis kit (Tailing Reaction) (B532451-0020, Sangon Biotech Co., Ltd, Shanghai, China) according to manufacturer's instructions. Briefly, a 20-μL reaction containing total RNA (1 μg), 2× miRNA P-RT Solution mix (10 μL), miRNA P-RT Enzyme mix (2 μL), and RNase-free H_2O (to 20 μL) was incubated at 37 °C for 60 min and then 85 °C for 5 min for reverse transcription. qPCR was performed using a step-one real-time PCR detection system (Thermo Fisher Scientiffc, Waltham, MA, USA), and data were collected with StepOne software (v2.2.3). Briefly, a total volume of 20 μL containing cDNA template (1 μL), forward primer (0.4 μL, 10 μM), reverse primer (0.4 μL, 10 μM), 2× Q3 SYBR qPCR Master Mix (10 μL, 22204, Tolo Biotech Co., Ltd, Shanghai, China), and RNase-free H_2O (8.2 μL) was prepared. The PCR program included an initial heating at 95 °C for 30 s, followed by 40 cycles of 95 °C for 10 s and 60 °C for 30 s. The relative amount of target mRNA under targeting versus non-targeting conditions was normalized to the level of *GAPDH*, and calculated as delta-delta threshold cycle (ΔΔCt). All the primers used for qPCR reactions are listed in Supplementary Data 6.

RNA-sequencing and off-target analysis

To determine the targeting specificity of STAR, RNA sequencing analysis was conducted. HEK293T cells were plated in 24-well plates and transfected with 200 ng of d*Ec*Cas6-toxin and 400 ng of bgCBS plasmids, 300 ng of *Rfx*Cas13d and 400 ng of sgRNA plasmids, and 500 ng of shRNA plasmids. Following a 48-h incubation, total RNA was extracted and 1 μg of total RNA was utilized for library preparation. RNA-sequencing was conducted on an Illumina HiSeq using a 2×150 paired-end configurations by GENEWIZ. For data analysis, fastq data were processed with Cutadapt (v1.9.1, phred cutoff: 20, error rate: 0.1, adapter overlap: 1 bp, min. length: 75, proportion of N: 0.1) to convert high-quality clean data. Then, clean data were aligned to reference genomes using Hisat2 (v2.2.1). Gene expression levels were estimated with HTSeq (v0.6.1), and differential expression analysis was performed using DESeq2 (v1.48.1). The adjusted p-value (padj) threshold was set to 0.05 to identify differentially expressed genes.

AAV production and infection

HEK293T cells were cultured in 10 cm dishes using DMEM supplemented with 10% FBS and 1% P/S. The day before transfection, cells were split at a ratio of 1:3. Each plate was transfected with 5 μg of pAAV-STAR, 5 μg of pHelper, 5 μg of rep/cap plasmid, and 24 μL of Lipo8000™. AAV particles were purified using a universal virus concentration kit (C2901M, Beyotime Biotech Co., Ltd, Nantong, China) according to the manufacturer's instructions after 72 h transfection. Briefly, cells were scraped and centrifuged at 4 °C for 10 min at 1150 *g*. The resulting precipitate was resuspended in 500 μL of PBS and lysed by repeated freezing and thawing in liquid nitrogen, followed by incubation in a 37 °C water bath. The lysate was then centrifuged at 4 °C for 10 min at 1150 *g*. The supernatant was combined with previously stored supernatant and incubated with 1× virus precipitation reagent at 4 °C overnight. After incubation, the cell lysates were centrifuged at 4 °C for 45 min at 1150 *g*. The supernatant was discarded, and 200 μL of viral resuspension solution containing a virus protection reagent was added and incubated for 10 min. The precipitate was then resuspended and centrifuged at 4 °C for 5 min at 12,000 *g*, and the supernatant containing viral particles was carefully aspirated under sterile conditions. The purified viral particles were quantified using qPCR and stored at -80 °C until use for infection. HEK293T or HepG2 cells were infected at the indicated MOI, and using AAV-DJ-GFP as an indicator of infection efficiency. Total RNA was extracted 48 h post-infection, followed by RT-qPCR to evaluate target RNA knockdown efficiency.

Western blotting

To assess the degradation efficiency of STAR at the protein level, HepG2 cells were seeded on 24-well plates and infected with AAV-DJ particles. After 48 hours, the cells were washed twice with ice-cold PBS and lysed in 80 μL of 2× SDS lysis buffer (50 mM Tris, 150 mM NaCl, 0.5% deoxycholate, 2% SDS, pH 7.4) followed by heating at 100 °C for 10 min. A 9% SDS-PAGE gel was prepared using the standard protocol, and 5 μL of cell samples were loaded into each well after the SDS-PAGE gel had solidified. Electrophoresis was conducted in 1× SDS running buffer (25 mM Tris, 192 mM glycerol, and 0.10% SDS, pH 8.3) at 100 V for approximately 90 min until the dye reached the bottom. The proteins were then transferred onto a PVDF membrane in 1× transfer buffer (25 mM Tris and 192 mM glycerol, pH 8.3) at 200 mA for 70 min, and then blocked in 5% BSA for 90 min. The membrane was cut along the marker sites according to the protein sizes, then incubated overnight at 4 °C with 10 mL of anti-MYC antibody (1:2000, Diagbio, db14926, Lot# W0616P) and anti-GapDH antibody (1:20000, Diagbio, db11729, Lot# W0510P), respectively. After three washes with TBST (15 mM NaCl, 1 mM Tris, and 0.1% Tween20, pH 8.0), the membrane was incubated with 10 mL of anti-HRP-conjugated antibody (1:2000, Servicebio, GB23303, Lot# AC2403303166) for 60 min. The membrane was then washed three times with TBST and imaged using LumiQ universal ECL luminescent liquid (ShareBio, SB-WB012) with a multi-functional fluorescence chemical imaging system (CLINX). The image was collected with CLINX Image Capture software (v6.0), and bands were quantified using CLINX Image Analysis software (v6.0).

Cell viability and proliferation assay

To determine the cytotoxicity of selected d*Ec*Cas6-toxins, HEK293T cells were seeded in 96-well plates and transfected with 100 ng of different d*Ec*Cas6-toxin plasmids for 48 h. To assess cell proliferation, HepG2 cells were seeded in 96-well plates and infected with *MYC*-targeting AAV-DJ particles for 72 h. Then, the medium was replaced with fresh medium supplemented with 10 µL of cell counting kit-8 (CCK-8) reagent (AKCE001, Beijing Boxbio Science &Technology Co., Ltd, Beijing, China) and incubated for 1 h in a 37 °C incubator. The absorbance was measured at 450 nm using a microplate reader, and data were collected with Gene 5 software (v3.04).

Cell apoptosis assay

After infecting HepG2 cells with AAV-DJ particles for 72 h, the cells were treated with trypsin and PBS and measured by the Annexin V-FITC/PI apoptosis detection kit (Cat No.40302ES20, Yeasen Biotech Co., Ltd, Shanghai, China) according to the manufacturer's instructions. Briefly, cells were re-suspended with 100 µL of 1× binding buffer. A 5 µL of Annexin V-FITC and 10 µL of PI staining solutions were then added to the cell suspension with gentle mixing, and incubated for 15 min followed by treatment with 400 µL of 1× binding buffer. The samples were analyzed with a flow cytometer using CytExpert (v2.3). For each sample, 10,000 individual cells which appeared in the live-cell gate were collected at a slow rate, and data were analyzed using the FlowJo software (v10.8.1).

Statistics and reproducibility

All data were analyzed using the GraphPad Prism software (v8.0.1). Data were presented as mean ± s.e.m. with $n = 3$ from three independent experiments. Statistical significances were defined as: $^{****}P < 0.0001$, $^{***}P < 0.001$, $^{**}P < 0.01$, $^{*}P < 0.05$, ns: not significant ($P > 0.05$). In this study, no statistical method was used to predetermine sample size, and no data were excluded from the analyses. The experiments were not randomized and the Investigators were not blinded to allocation during experiments and outcome assessment.

Reporting summary

Further information on research design is available in the Nature Portfolio Reporting Summary linked to this article.

Data availability

The RNA-seq data generated in this study have been deposited in the SRA under BioProject PRJNA1189810. The data generated in this study are provided in the Source Data file. Source data are provided with this paper.

References

1. Tavernier, G. et al. mRNA as gene therapeutic: how to control protein expression. *J. Control. Release* **150**, 238–247 (2011).
2. Wang, W. et al. Nucleic-acid-based targeted degradation in drug discovery. *J. Med. Chem.* **65**, 10217–10232 (2022).
3. Carthew, R. W. & Sontheimer, E. J. Origins and mechanisms of miRNAs and siRNAs. *Cell* **136**, 642–655 (2009).
4. Zeng, Y. & Cullen, B. R. RNA interference in human cells is restricted to the cytoplasm. *RNA* **8**, 855–860 (2002).
5. Scherer, L. J. & Rossi, J. J. Approaches for the sequence-specific knockdown of mRNA. *Nat. Biotechnol.* **21**, 1457–1465 (2003).
6. Jackson, A. L. et al. Expression profiling reveals off-target gene regulation by RNAi. *Nat. Biotechnol.* **21**, 635–637 (2003).
7. Birmingham, A. et al. 3′ UTR seed matches, but not overall identity, are associated with RNAi off-targets. *Nat. Methods* **3**, 199–204 (2006).
8. Wang, Y. et al. A biologically stable DNAzyme that efficiently silences gene expression in cells. *Nat. Chem.* **13**, 319–326 (2021).
9. Tong, Y. et al. Programming inactive RNA-binding small molecules into bioactive degraders. *Nature* **618**, 169–179 (2023).
10. Colognori, D., Trinidad, M. & Doudna, J. A. Precise transcript targeting by CRISPR-Csm complexes. *Nat. Biotechnol.* **41**, 1256–1264 (2023).
11. Ozcan, A. et al. Programmable RNA targeting with the single-protein CRISPR effector Cas7-11. *Nature* **597**, 720–725 (2021).
12. Abudayyeh, O. O. et al. RNA targeting with CRISPR-Cas13. *Nature* **550**, 280–284 (2017).
13. Smargon, A. A. et al. Cas13b is a Type VI-B CRISPR-associated RNA-guided RNase differentially regulated by accessory proteins Csx27 and Csx28. *Mol. Cell* **65**, 618–630 (2017).
14. Tong, H. et al. High-fidelity Cas13 variants for targeted RNA degradation with minimal collateral effects. *Nat. Biotechnol.* **41**, 108–119 (2023).
15. Qi, T. et al. Phage-assisted evolution of compact Cas9 variants targeting a simple NNG PAM. *Nat. Chem. Biol.* **20**, 344–352 (2024).
16. Kim, D. Y. et al. Hypercompact adenine base editors based on a Cas12f variant guided by engineered RNA. *Nat. Chem. Biol.* **18**, 1005–1013 (2022).
17. Wu, T. et al. An engineered hypercompact CRISPR-Cas12f system with boosted gene-editing activity. *Nat. Chem. Biol.* **19**, 1384–1393 (2023).
18. Xu, C. L. et al. Programmable RNA editing with compact CRISPR-Cas13 systems from uncultivated microbes. *Nat. Methods* **18**, 499–506 (2021).
19. Kannan, S. et al. Compact RNA editors with small Cas13 proteins. *Nat. Biotechnol.* **40**, 194–197 (2022).
20. Zhao, F. et al. A strategy for Cas13 miniaturization based on the structure and AlphaFold. *Nat. Commun.* **14**, 5545 (2023).
21. Batra, R. et al. Elimination of toxic microsatellite repeat expansion RNA by RNA-targeting Cas9. *Cell* **170**, 1–14 (2017).
22. Liu, H. C., Rauch, S. & Dickinson, B. C. Programmable technologies to manipulate gene expression at the RNA level. *Curr. Opin. Chem. Biol.* **64**, 27–37 (2021).
23. Rauch, S. et al. Programmable RNA-guided RNA effector proteins built from human parts. *Cell* **178**, 122–134 (2019).
24. Han, Y. & Lee, E. J. Substrate specificity of bacterial endoribonuclease toxins. *BMB Rep.* **53**, 611–621 (2020).
25. LeRoux, M. & Laub, M. T. Toxin-antitoxin systems as phage defense elements. *Annu. Rev. Microbiol.* **76**, 21–43 (2022).
26. Mossakowska, D. E., Nyberg, K. & Fersht, A. R. Kinetic characterization of the recombinant ribonuclease from Bacillus amyloliquefaciens (barnase) and investigation of key residues in catalysis by site-directed mutagenesis. *Biochemistry* **28**, 3843–3850 (1989).
27. Fujita, Y. et al. A versatile and robust cell purification system with an RNA-only circuit composed of microRNA-responsive ON and OFF switches. *Sci. Adv.* **8**, eabj1793 (2022).
28. Jackson, R. N. et al. Crystal structure of the CRISPR RNA-guided surveillance complex from *Escherichia coli*. *Science* **345**, 1473–1479 (2014).
29. Haurwitz, R. E. et al. Sequence- and structure-specific RNA processing by a CRISPR endonuclease. *Science* **329**, 1355–1358 (2010).
30. Niewoehner, O., Jinek, M. & Doudna, J. A. Evolution of CRISPR RNA recognition and processing by Cas6 endonucleases. *Nucleic Acids Res.* **42**, 1341–1353 (2014).
31. Mitkas, A. A., Valverde, M. & Chen, W. Dynamic modulation of enzyme activity by synthetic CRISPR-Cas6 endonucleases. *Nat. Chem. Biol.* **18**, 492–500 (2022).
32. Qi, L. et al. RNA processing enables predictable programming of gene expression. *Nat. Biotechnol.* **30**, 1002–1006 (2012).
33. DiAndreth, B. et al. PERSIST platform provides programmable RNA regulation using CRISPR endoRNases. *Nat. Commun.* **13**, 2582 (2022).

34. Li, W. et al. An improved imaging system that corrects MS2-induced RNA destabilization. *Nat. Methods* **19**, 1558–1562 (2022).
35. Meiering, E. M., Serrano, L. & Fersht, A. R. Effect of active site residues in barnase on activity and stability. *J. Mol. Biol.* **225**, 585–589 (1992).
36. Yu, V. et al. MqsR is a noncanonical microbial RNase toxin that is inhibited by antitoxin MqsA via steric blockage of substrate binding. *J. Biol. Chem.* **298**, 102535 (2022).
37. Liu, R. et al. Optogenetic control of RNA function and metabolism using engineered light-switchable RNA-binding proteins. *Nat. Biotechnol.* **40**, 779–786 (2022).
38. Choudhury, R. et al. Engineering RNA endonucleases with customized sequence specificities. *Nat. Commun.* **3**, 1147 (2012).
39. Li, G. et al. Characterization of dual substrate binding sites in the homodimeric structure of *Escherichia coli* mRNA interferase MazF. *J. Mol. Biol.* **357**, 139–150 (2006).
40. Wessels, H. H. et al. Massively parallel Cas13 screens reveal principles for guide RNA design. *Nat. Biotechnol.* **38**, 722–727 (2020).
41. Bofill-De Ros, X. & Gu, S. Guidelines for the optimal design of miRNA-based shRNAs. *Methods* **103**, 157–166 (2016).
42. Yin, H., Kauffman, K. J. & Anderson, D. G. Delivery technologies for genome editing. *Nat. Rev. Drug Discov.* **16**, 387–399 (2017).
43. Lerch, T. F. et al. Structure of AAV-DJ, a retargeted gene therapy vector: cryo-electron microscopy at 4.5 Å resolution. *Structure* **20**, 1310–1320 (2012).
44. Wang, C. et al. Alternative approaches to target Myc for cancer treatment. *Signal Transduct. Target Ther.* **6**, 117 (2021).
45. Llombart, V. & Mansour, M. R. Therapeutic targeting of "undruggable" MYC. *EBioMedicine* **75**, 103756 (2022).
46. Abudayyeh, O. O. et al. C2c2 is a single-component programmable RNA-guided RNA-targeting CRISPR effector. *Science* **353**, aaf5573 (2016).
47. Huynh, N. et al. A versatile toolkit for CRISPR-Cas13-based RNA manipulation in *Drosophila*. *Genome Biol.* **21**, 279 (2020).
48. Tian, R. Z. et al. Establishing a synthetic orthogonal replication system enables accelerated evolution in *E. coli*. *Science* **383**, 421–426 (2023).
49. Doman, J. L. et al. Phage-assisted evolution and protein engineering yield compact, efficient prime editors. *Cell* **186**, 3983–4002.e26 (2023).

Acknowledgements

This work was jointly supported by the National Key Research and Development Program of China (Grant 2024YFA0917100 to B.C.Ye), the National Natural Science Foundation of China (Grants 22374047 to B.C.Yin, Grants 22134003 to B.C.Ye), and the Fundamental Research Funds for the Central Universities (B.C.Yin). We thank Prof. Chen Ling and Dr. Yun He (State Key Laboratory of Genetic Engineering and Engineering Research Center of Gene Technology (Ministry of Education), School of Life Sciences, Zhongshan Hospital, Fudan University, Shanghai, China) for giving the AAV-DJ plasmids and guiding the AAV experiments.

Author contributions

P.R.C. and B.C. Yin conceived, designed the experiments. P.R.C., P.P.Q., Y.N.W., P.F.L., X.Y.Z., and T.Q. performed and analysed the experiments. B.C. Yin and B.C. Ye supervised and discussed the experiments with P.R.C., B.C. Yin, and P.R.C. wrote the manuscript.

Competing interests

The authors declare no competing interests.

Additional information

Supplementary information The online version contains supplementary material available at https://doi.org/10.1038/s41467-025-63166-y.

Correspondence and requests for materials should be addressed to Bang-Ce Ye or Bin-Cheng Yin.

Peer review information *Nature Communications* thanks Sigitas Mikutis and the other, anonymous, reviewer(s) for their contribution to the peer review of this work. A peer review file is available.